Indian Journal of Pure & Applied Physics
Vol. 59, August 2021, pp. 549-558

Impedance and Electric Modulus Spectroscopy of Polycrystalline $La_{0.5}Sr_{0.5}Bi_{0.2}Co_{0.4}Fe_{0.4}O_{3-\delta}$ Cathode Ceramic for Intermediate Temperature SOFCs

Sunder Singh[a], Manindra Kumar[b], Anil Kumar[a], Deepash Shekhar Saini[b*]

[a]Department of Physics, Hindu college Moradabad, Moradabad, India-244 001
[b]Department of Physics, Deen Dayal Upadhyaya Gorakhpur University, Gorakhpur, India-273 009

Received 9 May 2021; accepted 7 July 2021

In the present research work, $La_{0.5}Sr_{0.5}Bi_{0.2}Co_{0.4}Fe_{0.4}O_{3-\delta}$ cathode ceramic powder is synthesized through cost-effective flash pyrolysis process and followed by conventional sintering for IT-SOFCs. The Rietveld refinement program is used to determine the crystal structure, unit cell parameters and bond length. The XRD result indicates existence of a pure single phase of rhombohedral structure with $R\bar{3}C$ space group symmetry detected from the sample sintered at 700 ℃. FESEM micrographs of fracture surface of sample sintered at 700 ℃ showed a high porosity and nano grain sizes (50-100 *nm*). Combined impedance and electric modulus spectroscopic are used to investigate the relaxation phenomena in $La_{0.5}Sr_{0.5}Bi_{0.2}Co_{0.4}Fe_{0.4}O_{3-\delta}$ ceramic over a broad range of temperature and frequency. A single relaxation peak is observed in the imaginary part of impedance and electric modulus spectra, which could be due to the contribution of grain boundary of $La_{0.5}Sr_{0.5}Bi_{0.2}Co_{0.4}Fe_{0.4}O_{3-\delta}$ ceramic. The imaginary part of modulus (M'') spectra is studied with help of non-exponential decay function or Kohlrausch–Williams–Watts (KWW) parameter (β). In the combined plot of the imaginary part of impedance (Z'') and electric modulus (M'') spectra at 210 ℃, only a single peak of $Z''$and M'' is observed at the same frequency which specifies that the conduction process is a long-range motion of the charge carriers. The frequency-dependent conductivity is followed by the Jonscher's double power law in the temperature range 30-210 ℃.

Keywords: Cathode materials; Grain boundary; Porous; Impedance; Electric modulus; Jonscher's double power law

1 Introduction

Solid Oxide Fuel Cell (SOFC) is a third-generation fuel cell, which converts the chemical energy directly into the electrical energy at the intermediate and high temperatures[1,2]. In recent years, SOFCs have attained a lot of attention due to one of the most efficient, pollution free, clean, and eco-friendly advanced fuel cells. SOFCs have several advantages over other traditional energy systems including hydro, nuclear and fossil fuels like highly efficient, fuel flexible, reliable and source of negligible emission of NO_x and SO_x[3,4]. Hence, there is much devotion to develop cathode and electrolyte materials with longer life and high conductivities in the temperature range of 500 ℃ to 700 ℃, which reduced the cost of the cell as well as increased the cell life because of utilization of alloys as interconnections compare to ceramics at the relatively low temperature[5].

In SOFCs, the role of cathode offers the sites for the electrochemical reduction of oxygen. For this, the cathode must have: (1) excellent ionic and electronic conductivity over a wide range of the temperature; (2) an identical thermal expansion coefficient (TEC) and chemical compatibility with the electrolyte and interconnecting materials; (3) sufficient porosity for allowing gaseous oxygen to readily diffuse through the cathode to the cathode/electrolyte interface; (4) stability under an oxidizing atmosphere during fabrication and working; (5) highly active catalyst for the oxygen reduction reaction (ORR); and (6) low cost. Mixed ionic and electronic conductors (MIECs) with high ionic as well as high electronic conductivities have been considered as an ideal cathode for IT-SOFCs due to relatively low cathodic polarization resistance when we extend the active zone of the reaction from the three-phase boundary (TPB) in the cathode-gas interface[6-8]. Therefore, the production and development of alternative cathode materials which are highly active electro catalysts on oxygen reduction reactions (ORR) to reduce the polarization resistance at the cathode/electrolyte interface is mainly desirable[9].

To explore the new cathode materials for SOFCs, several studies and efforts have been made for developing the new materials. In particular, perovskites are important due to having high ionic

*Corresponding author: (E-mail: dssainiddugu@gmail.com)

and electronic conductivity and high oxygen surface exchange coefficient[10]. Due to their strong catalytic activity for the oxygen reduction reaction, as well as high ionic and electronic conductivity, the $La_{1-x}Sr_xCo_{1-y}Fe_yO_{3-\delta}$ (LSCF) perovskites have been identified as viable cathode materials to replace the traditional $La_{1-x}Sr_xMnO_{3-\delta}$ (LSM) cathode materials[11,12]. However, the instability of thermal expansion coefficient of LSCF with electrolyte is serious problem[13,14]. Furthermore, on the basis of the previous studies, substitution of bismuth in LSCF is helpful to increase the stability, oxygen permeation as well as compatibility the thermal expansion coefficient of this perovskite. For example, Sunarso *et al.* reported that the oxygen permeation and phase stability is increased by the substitution of Bi in $BaSc_{0.1}Co_{0.9}O_{3-\delta}$ perovskite[15]. Similarly, Li *et al.*[16] showed increasing oxygen permeation flux with the increase of Bi content in $Sr_{10-n/2}Bi_{n/2}Fe_{20}O_m$ and $Sr_{1-x}Bi_xFeO_3$. Sheo *et al.*[17] indicated in their study that oxygen permeation is increased when Bi is added to $BaCoO_{3-\delta}$ perovskite and stated that a small amount of Bi is necessary to control the thermal expansion coefficient of this type perovskite. However, many researchers are primarily focused on particular specific characteristics related to the SOFCs application in order to produce LSCF cathode materials. The complete investigation of electrical characteristics of LSCF cathode materials utilising impedance and electric modulus spectroscopy receives little attention. Impedance and modulus spectroscopy is an extremely useful method for determining transport characteristics, relaxations, grain contribution, grain boundary effects, and electrode effects. In this context, $La_{0.5}Sr_{0.5}$ $Bi_{0.2}Co_{0.4}$ $Fe_{0.4}O_{3-\delta}$ nanocrystalline ceramic powder synthesized by flash pyrolysis (FP) route followed by conventional sintering. Impedance and modulus spectroscopy have been performed for $La_{0.5}Sr_{0.5}$ $Bi_{0.2}Co_{0.4}Fe_{0.4}O_{3-\delta}$ ceramic to get a comprehensive understanding of its electrical properties for IT-SOFCs.

2 Experimental details

A flash pyrolysis route is used to synthesis nano-sized $La_{0.5}Sr_{0.5}Bi_{0.2}Co_{0.4}Fe_{0.4}O_{3-\delta}$ powders [18,19] using high purity (>99%) raw materials: $La(NO_3)_3.6H_2O$, $Sr(NO_3)_2$, $Bi(NO_3)_2.5H_2O$, $Co(NO_3)_2.5H_2O$ and $Fe(NO_3)_3.9H_2O$ (Alfa Aesar). At first, a clear aqueous solution of $La(NO_3)_3.6H_2O$, $Sr(NO_3)_2$, $Bi(NO_3)_2.5H_2O$, $Co(NO_3)_2.5H_2O$ and $Fe(NO_3)_3.9H_2O$ of 0.5 *M*are made by adding distilled water in the appropriate proportions.Using a magnetic stirrer, the stoichiometric volume of aqueous solutions is mixed in a 2000 *mL* beaker, and the appropriate amount of citric acid is applied to the above metal ion solution. Citric acid and metal ions are mixed in a ratio of 1.5:1. With the aid of a dilute NH4OH solution, the pH of the above solution is adjusted to 7. It is then added the appropriate amounts of glycine (metal ions: glycine = 1:0.5) and ethylene glycol (metal ions: ethylene glycol = 1:1.5). To begin with, citric acid and glycine serve as chelating agents, but they also serve as fuel during the combustion process. The resulting solution is placed in a pit furnace and heated to 350 °*C* using infrared heating from the top surface. The incremental evaporation of water results in the formation of a gel. Finally, due to a spontaneous combustion in the gel, the gel is transformed into a low-density black fuzzy mass. Since, the as-prepared powder incorporates carbon and other organic impurities obtained via the flash pyrolysis route, it is calcined at 600 °*C* in an alumina crucible for 2 hrs in the air to produce $La_{0.5}Sr_{0.5}Bi_{0.2}Co_{0.4}Fe_{0.4}O_{3-\delta}$ powder in the form of nano-sized particles. The organic component of the as-prepared powder is burned out in the air during the heat treatment, resulting in ultrafine powder. The $La_{0.5}Sr_{0.5}Bi_{0.2}Co_{0.4}Fe_{0.4}O_{3-\delta}$ powder is calcined at 600 °*C* for 2*h* before being crushed with an agate mortar and pestle for 15 min to obtain a fine powder. The binder solution (polyvinyl alcohol (PVA)) is then mixed with crushed powder to improve the compactness of the materials' granules, and then squeezed uniaxially in a steel die under 340 *MPa* pressure for 1 *min*. in a hydraulic press to produce $La_{0.5}Sr_{0.5}Bi_{0.2}Co_{0.4}Fe_{0.4}O_{3-\delta}$ perovskite powder pellets. Densification of compacted powder samples (green bodies) in a continuous 3D structure is now needed. The green $La_{0.5}Sr_{0.5}Bi_{0.2}Co_{0.4}Fe_{0.4}O_{3-\delta}$ pellets are sintered at 700 °*C*.

The X-ray diffractometer of the Bruker D8 Advance device is used within 20° to 80° with a step size of 0.019° to identify the phase of $La_{0.5}Sr_{0.5}$ $Bi_{0.2}Co_{0.4}Fe_{0.4}O_{3-\delta}$. The field emission scanning electron microscope (FESEM) from Zeiss (Merlin-Gemini II) is used to study the microstructure of sintered samples, such as grain morphology and grain size. Impedance spectroscopy was used with a broad range of temperature (30 - 210 °*C*) and frequency (50 *Hz* – 5 *MHz*) at environmental atmosphere to investigate the sources of the electrical properties of $La_{0.5}Sr_{0.5}Bi_{0.2}Co_{0.4}Fe_{0.4}O_{3-\delta}$ ceramic. To make the

Ag-$La_{0.5}Sr_{0.5}Bi_{0.2}Co_{0.4}Fe_{0.4}O_{3-\delta}$-Ag symmetric cell structure, silver paste was used.

3 Result and Discussion

Structural and microstructural behaviors of $La_{0.5}Sr_{0.5}Bi_{0.2}Co_{0.4}Fe_{0.4}O_{3-\delta}$

The structural and phase purity of $La_{0.5}Sr_{0.5}Bi_{0.2}Co_{0.4}Fe_{0.4}O_{3-\delta}$ ceramic sintered at 700 °*C* for 2*h* has been studied through XRD technique and presented in Fig. 1. The XRD pattern of $La_{0.5}Sr_{0.5}Bi_{0.2}Co_{0.4}Fe_{0.4}O_{3-\delta}$ indicates the phase purity of $La_{0.5}Sr_{0.5}Bi_{0.2}Co_{0.4}Fe_{0.4}O_{3-\delta}$ ceramic. The peaks of the XRD pattern of $La_{0.5}Sr_{0.5}Bi_{0.2}Co_{0.4}Fe_{0.4}O_{3-\delta}$ ceramics sintered at 700 °*C* for 2*h* are well matched with JCPDF file number 49-0283[20]. We have performed the Rietveld refinement of the XRD pattern by assuming rhombohedral crystal system with $R\bar{3}C$ space group, and the results are presented in Fig. 1(a). The unit cell parameters extracted from Rietveld refinement of the XRD pattern are found a = b = 5.581550 *Å* and c = 13.392042 *Å*, which are excellent agreement with literature[20] and increased with the increasing content of Fe as compare with our previously reported result for $La_{0.5}Sr_{0.5}Bi_{0.2}Co_{0.5}Fe_{0.3}O_{3-\delta}$[19]. The refined structural parameters and atomic positions are tabulated in Table 1 and Table 2, respectively. The crystallite size of $La_{0.5}Sr_{0.5}Bi_{0.2}Co_{0.4}Fe_{0.4}O_{3-\delta}$ ceramic is calculated by Debye-Scherrer's formula using its XRD pattern and found 29.78 nm. It also seems that the crystallite size is increased with the increasing content of Fe if we compare to our previously reported result for $La_{0.5}Sr_{0.5}Bi_{0.2}Co_{0.5}Fe_{0.3}O_{3-\delta}$ [19]. The CIF file of XRD pattern is generated using Fullprof program. The rhombohedral structure of the unit cell of sintered $La_{0.5}Sr_{0.5}Bi_{0.2}Co_{0.4}Fe_{0.4}O_{3-\delta}$ ceramic is drawn by using the Diamond software and has been shown in Fig. 1(b).

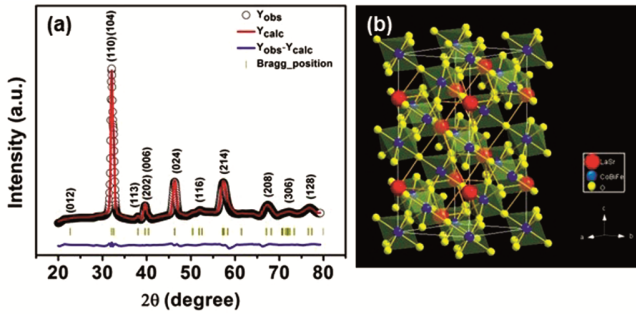

Fig. 1 — (a). Rietveld refine XRD of sintered $La_{0.5}Sr_{0.5}Bi_{0.2}Co_{0.4}Fe_{0.4}O_{3-\delta}$, and (b). Refine structure of $La_{0.5}Sr_{0.5}Bi_{0.2}Co_{0.4}Fe_{0.4}O_{3-\delta}$ pellet sintered at 700 °C for 2*h* in air.

Furthermore, the microstructure of fracture surface of $La_{0.5}Sr_{0.5}Bi_{0.2}Co_{0.4}Fe_{0.4}O_{3-\delta}$ sintered pellet at 700 °*C* is investigated through FESEM and shown in Fig. 2 (a-b). The microstructure of sintered pellet has fine spherical grain and highly porous, and an inter granular fracture mode is observed in the sample. If we compare this result with our previously reported result of $La_{0.5}Sr_{0.5}Bi_{0.2}Co_{0.5}Fe_{0.3}O_{3-\delta}$ ceramic, it is found that the microstructure is same but differ in the relative density *i.e.* relative density is decreased with the increasing amount of Fe. The decrease in relative density suggests lower cation diffusion rates with increasing substitution Fe content in ceramic[19].

Impedance analysis

The Nyquist plots (Z'' *vs* Z') of sintered $La_{0.5}Sr_{0.5}Bi_{0.2}Co_{0.4}Fe_{0.4}O_{3-\delta}$ ceramic at the selected temperatures are presented in Fig. 3(a-b). These Z'' *vs* Z' plots are consisted of a single semi-circular

Table 1 — Refined structural parameters for $La_{0.5}Sr_{0.5}Bi_{0.2}Co_{0.4}Fe_{0.4}O_{3-\delta}$ heated at 700 °*C*.

T (°*C*)	Unit Cell Parameters (*Å*)	Volume ($Å^3$)	Rietveld Refined Parameters	Bond length (*Å*) La/Sr-O	Co/Fe/Bi-O	Crystallite size (*nm*)
700	a = 5.58155 b = 5.58155 c =13.39204	361.32	R_p= 13.5, R_{wp}= 23.9 R_{exp} =17.84, χ^2 = 1.79	2.4151	1.9957	29.78

Table 2 — Atomic positions and occupancies of $La_{0.5}Sr_{0.5}Bi_{0.2}Co_{0.4}Fe_{0.4}O_{3-\delta}$(Rhombohedral crystal system with $R\bar{3}C$ space group symmetry).

Atom	Wyckoff position	x/a	y/b	z/c	Occ	U [$Å^2$]
La1	6a	0	0	1/4	0.5	0.0189
Sr2	6a	0	0	1/4	0.5	0.0189
Co3	6b	0	0	0	0.4	0.1270
Fe4	6b	0	0	0	0.4	0.1270
Bi5	6b	0	0	0	0.2	0.1270
O6	18e	0.4327	0	1/4	1.0	0.0937

arc in the temperature range 30 – 210 ℃. The appearances of single arc in Z'' vs Z' plots are due to the contribution of grain boundary only and reveals only the presences of one types of relaxation mechanism with the sufficiently different relaxation times[21, 22]. The size of the semicircular arc decreases with temperature from 30 to 90 ℃ and then increases with temperature from 110 to 210 ℃. This may be associated with the phase transition of $La_{0.5}Sr_{0.5}Bi_{0.2}Co_{0.4}Fe_{0.4}O_{3-\delta}$ ceramic. The centers of the semicircular arcs are not lied on the real axis which suggests the non-homogeneity and deviation from the ideal behavior of the sample[23]. Thus, considerable grain boundary effect with sufficiently different relaxation time is observed in the sample. Furthermore, the value of capacitance related to the grain boundary is observed to around 10^{-9}. Moreover, a ideal semicircle in the Nyquist plots suggests that the relaxation mechanism is Debye-type[24]. In this case, the departure from the ideal semicircular shape in the Nyquist plots reveals non-Debye type relaxation mechanism in the sample. The deformation of semicircle from the perfect semicircle in the Nyquist plots is represents the statistical distribution of relaxation times[25]. Therefore, the electrical mechanism is occurred in the sample have been modeled in the terms of the equivalent electrical circuit [R_s ($Q_{gb}R_{gb}$)] as shown in the inset of Fig. 3(a-b). Where, R_s is the series resistance of the interconnection, R_{gb} is the grain boundary resistance and Q_{gb} is the constant phase element corresponding to the grain boundary. In order to find out grain boundary resistance (R_{gb}) in the material at selected temperature, the experimental data were simulated according to the defined model circuit $R_s(Q_{gb}R_{gb})$ using Z simp Win software[26].

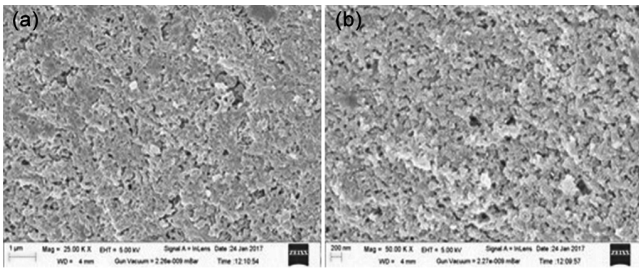

Fig. 2 — FESEM image with a magnification of (a) 25 KX and 50 KX for fracture surface of $La_{0.5}Sr_{0.5}Bi_{0.2}Co_{0.4}Fe_{0.4}O_{3-\delta}$ pellet sintered at 700 ℃ for 2h in air.

Therefore, the complex impedance can be presented by the Cole-Cole function[27, 28] for the contribution of grain interior, grain boundary and electrode polarization:

$$Z^* = {R_g}/{[1+(j\omega R_g C_g)^{\alpha_g}]} + {R_{gb}}/{[1+(j\omega R_{gb} C_{gb})^{\alpha_{gb}}]} + {R_e}/{[1+(j\omega R_e C_e)^{\alpha_e}]} \quad \ldots(1)$$

Where, R_g, R_{gb} and R_e represent the electrical resistance of the grain interior, grain boundary and electrode, respectively, while C_g, C_{gb} and $C_e$represent the value of the capacitance of the grain interior, grain boundary and electrode, respectively and α provides the information of the distribution of the relaxation times and its value are ranging from 0 to 1. The value of α is equal to unity and corresponding to the full width at half maximum (FWHM) of peak is 1.14 decade for a perfect Debye relaxation. Furthermore, $0 < \alpha < 1$ indicates that the relaxation phenomena is controlled by the distribution of relaxation times as a result which, broadening in the ideal Debye relaxation peak is observed. For the separation of the real (Z′) and imaginary (Z″) parts of Eq. (1), we can write

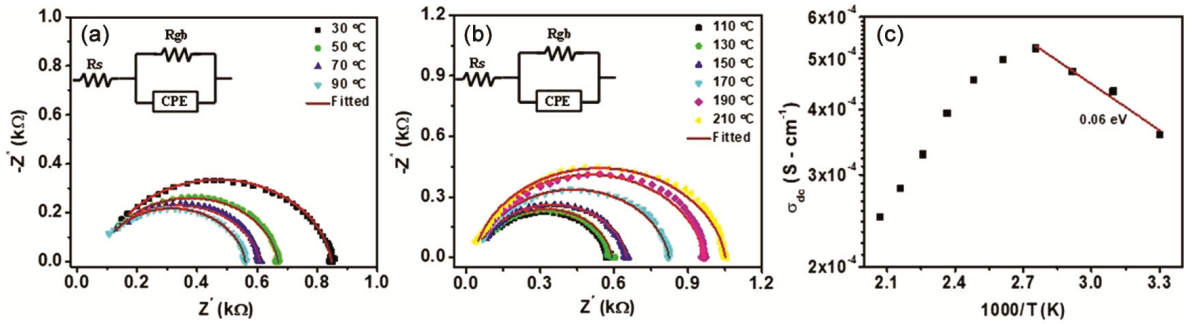

Fig. 3 — (a) Impedance plane plots (Nyquist plots) of $La_{0.5}Sr_{0.5}Bi_{0.2}Co_{0.4}Fe_{0.4}O_{3-\delta}$ ceramic in the temperature range 30-90 ℃, (b) Impedance plane plots of $La_{0.5}Sr_{0.5}Bi_{0.2}Co_{0.4}Fe_{0.4}O_{3-\delta}$ ceramic in the temperature range 110-210 ℃. Inset shows the equivalent circuit model and (c) the total dc conductivity of $La_{0.5}Sr_{0.5}Bi_{0.2}Co_{0.4}Fe_{0.4}O_{3-\delta}$ ceramic, the solid line is the best fit of Arrhenius relation.

$$Z' = \frac{R_g\{1+(\omega\tau_g)^{\alpha_g}\sin[(1-\alpha_g)\frac{\pi}{2}]\}}{1+(\omega\tau_g)^{2\alpha_g}\sin[(1-\alpha_g)\frac{\pi}{2}]} + \frac{R_{gb}\{1+(\omega\tau_{gb})^{\alpha_{gb}}\sin[(1-\alpha_{gb})\frac{\pi}{2}]\}}{1+(\omega\tau_{gb})^{2\alpha_{gb}}\sin[(1-\alpha_{gb})\frac{\pi}{2}]} + \frac{R_e\{1+(\omega\tau_e)^{\alpha_e}\sin[(1-\alpha_e)\frac{\pi}{2}]\}}{1+(\omega\tau_e)^{2\alpha_e}\sin[(1-\alpha_e)\frac{\pi}{2}]} \quad \ldots(2)$$

$$Z'' = \frac{R_g\{1+(\omega\tau_g)^{\alpha_g}\cos[(1-\alpha_g)\frac{\pi}{2}]\}}{1+(\omega\tau_g)^{2\alpha_g}\sin[(1-\alpha_g)\frac{\pi}{2}]} + \frac{R_{gb}\{1+(\omega\tau_{gb})^{\alpha_{gb}}\cos[(1-\alpha_{gb})\frac{\pi}{2}]\}}{1+(\omega\tau_{gb})^{2\alpha_{gb}}\sin[(1-\alpha_{gb})\frac{\pi}{2}]} + \frac{R_e\{1+(\omega\tau_e)^{\alpha_e}\cos[(1-\alpha_e)\frac{\pi}{2}]\}}{1+(\omega\tau_e)^{2\alpha_e}\sin[(1-\alpha_e)\frac{\pi}{2}]} \quad \ldots(3)$$

From the above, it can be concluded from the complex impedance data that only grain boundary contribution was observed in the temperature range of 30-210 °*C*. Therefore, only second term in Eq. (1) is essential to fit the complex impedance data. It is also obvious from the complex impedance data, which are completely well fitted in the experimental range of frequencies and temperatures. The fitting parameters are also tabulated in the Table 3(a-b). As shown in Table 3(a) the value of n_{gb} depends on the temperature and less than unity.

Indeed, the impedance spectroscopy is used as a non-devastating technique that used to separate the grain interior and grain boundary effect due to sufficiently different relaxation frequencies in the grain interior and grain boundary. This technique also allowed to find out the activation energy corresponding to the grain interior and grain boundary of the materials during the electrical conduction process and distinguish the type of impurities in the materials[29]. The dc conductivity is deduced in the term of the resistance extract from the complex impedance data through the accounting the sample geometry according to the Eq. 4:

$$\sigma = \frac{L}{A}\left[\frac{1}{R_{gb}}\right] \quad \ldots(4)$$

$$\sigma_{dc} = \sigma_o exp\left[\frac{-E_a}{kT}\right] \quad \ldots(5)$$

Where, L is the thickness of the sample, A is the area of the sample and R_{gb} is the resistance of the grain boundary. The dc conductivity is plotted as a function of the inverse of the temperature by using Eq. 5[30].

Where, σ_o is a pre-exponential factor, E_a is activation energy, k is the Boltzmann constant and T is the absolute temperature. The conductivity of sample is firstly increased with temperature up to 90 °*C* than decreased with temperature above 110 °*C*. The $\sigma_{dc}\ vs\ 1/T$ plot conformed the Arrhenius equation up to 90 °*C*, and the activation energy for the conduction of the charge carries in the material is deduced from the slope of the curve and to be observed 61 *meV*. This activation energy for conduction process is evidently indicates that the conduction mechanism up to 90 °*C* is electronic in nature[30].

The electronic conductivity is determined by the double exchange between the oxygen ions and ferric/cobalt ions, and the mechanistic model can be written as[31]

Table 3(a) — Electrical equivalent circuit [$R_s(Q_{gb}R_{gb})$] fitting parameters: series resistance (R_s), grain boundary resistance (R_{gb}), constant phase element corresponding to the grain boundary (Q_{gb}) and n_{gb} from impedance spectra for $La_{0.5}Sr_{0.5}Bi_{0.2}Co_{0\cdot5}Fe_{0.3}O_{3-\delta}$ ceramic in air.

Temperature (°C)	R_s (Ω)	R_{gb} (Ω)	Q_{gb} (S-sec^2)	n_{gb}
30	90.06	757	5.264×10^{-10}	0.9247
50	86.43	582	5.298×10^{-10}	0.9319
70	69.33	539	9.760×10^{-10}	0.9005
90	72.62	487	7.267×10^{-10}	0.9303
110	59.8	512	8.892×10^{-10}	0.9236
130	54.26	536	8.985×10^{-10}	0.9266
150	49.16	601	1.290×10^{-9}	0.9123
170	45.76	777	1.443×10^{-9}	0.9096
190	38.86	927	1.308×10^{-9}	0.9217
210	30.01	1022	1.723×10^{-9}	0.9097

Table 3(b) — The parameters obtained from the fitting of the imaginary part of complex electric modulus: KKW parameter (β), M''_{max} and f''_{max}.

Temperature (°C)	M''_{max}	f_{max} (Hz)	β
30	1.62×10^{-3}	3.07964×10^{6}	0.6378
50	1.50×10^{-3}	2.94071×10^{6}	0.7291
70	1.34×10^{-3}	2.71594×10^{6}	0.7744
90	1.09×10^{-3}	2.50389×10^{6}	0.7418
110	9.10×10^{-4}	1.98001×10^{6}	0.7780
130	7.91×10^{-4}	1.45853×10^{6}	0.8717
150	6.50×10^{-4}	1.16724×10^{6}	0.8322
170	5.07×10^{-4}	6.35455×10^{5}	0.9103
190	4.18×10^{-4}	4.67509×10^{5}	0.8733
210	3.81×10^{-4}	3.79932×10^{5}	0.9046

$Fe^{3+} - O^{2-} - Fe^{4+} - O^{2-} - Fe^{3+}$ ...(6)

$Co^{3+} - O^{2-} - Co^{4+} - O^{2-} - Co^{3+}$ ...(7)

The transport of the electrons along Fe^{3+}/Co^{3+}, O^{2-}, and Fe^{4+}/Co^{4+} contributes to the electronic conductivity. Since the content of Fe^{3+}/Co^{3+} is much higher than Fe^{4+}/Co^{4+}, the Fe^{4+}/Co^{4+} content determines the electronic conductivity.

The imaginary part of complex impedance as a function of frequency ($Z'' \, vs \, f$) at selected temperature for the $La_{0.5}Sr_{0.5}Bi_{0.2}Co_{0.4}Fe_{0.4}O_{3-\delta}$ ceramic is presented in Fig. 4(b) and the solid line is representing the fitting of the experimental data using the second term of Eq. (3). From the $Z'' \, vs \, f$ plots, it is clearly obvious that the nature and the shape of the plots are changed with the frequency as well as the temperature. In these graphs, a single peak is observed at a particular frequency $\omega_{max} = 2\pi f_{max}$. This frequency is called relaxation frequency such that $\omega_{max}\tau = 1$, where, τ is called the relaxation time constant. Furthermore, there is asymmetric broadening of the peaks reveals that the presence of electrical relaxation with a distribution of relaxation times in the materials. Moreover, the relaxation frequency (f_{max}) moves toward the higher frequency side with the increasing of the temperature up to 90 ℃ is mainly due to decrement in the resistance and then the relaxation frequency (f_{max}) shifts toward the lower frequency with the increasing of the temperature above 90 ℃ is mainly due to increment in the resistance[32]. This indicates that the number of the charge carriers (number of electrons which transport along Fe^{3+}/Co^{3+}, O^{2-}, and Fe^{4+}/Co^{4+}) are depleted in the conduction process due to the phase transition above 110 ℃. This single peak in the Z'' spectra are correlated to the grain boundary contribution. However, other peaks are not found in the Z" spectra may be associated with the grain interior response and electrode polarization[33]. Therefore, there is a considerable grain boundary effect on electrical relaxation behavior of the sample as observed in Nyquist plots.

The logarithmic of the relaxation time ($\tau_{Z''}$) of electrons which participate in double exchange between the oxygen ions and ferric/cobalt ions as a function of the reciprocal temperature ($1/T$) extract from $Z'' \, vs \, f$ plots are presents in the inset of Fig. 4(b). The plot is expressed by Arrhenius's equation up to 90 ℃[34]:

$$\tau_{Z''} = \tau_{oZ''} exp\left[\frac{E_{a\tau Z''}}{kT}\right] \quad ...(7)$$

Where, $E_{a\tau Z''}$ is the activation energy for conductive relaxation and $\tau_{oZ''}$ is characteristic relaxation time. An unique value of the activation energy ($E_{a\tau Z''}$) is found to 38 meV and characteristic relaxation time ($\tau_{oZ''}$) is observed to 4.042 ×10 $^{-8}$ *sec.* in 30 to 90 ℃ range of temperature.

Electric modulus analysis

Figure 5(a) shows the complex electric modulus plots (M'' vs M') for $La_{0.5}Sr_{0.5}Bi_{0.2}Co_{0.5}Fe_{0.3}O_{3-\delta}$ ceramic at selected temperatures. It is observed from the plots, a single distorted semi-circular arc, which is analogous to the Nyquist plots, is appeared in the measured frequency range and temperature range, which is mainly due to the contribution of grain boundary to the overall capacitive behavior of the sample. Furthermore, the canter of the arcs is not lie on the real axis reveals the deviation from the Debye-type dielectric relaxation. It is also observed that the

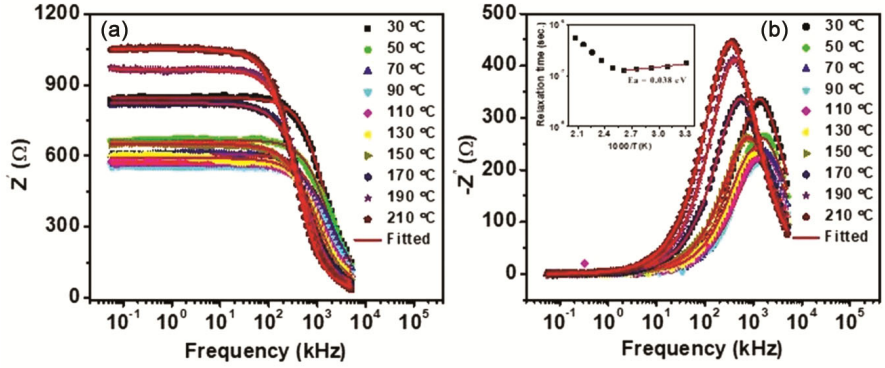

Fig. 4 — (a) The real part of impedance (Z′) and (b) the imaginary part of impedance (Z′′) as function of frequency at different temperature for $La_{0.5}Sr_{0.5}Bi_{0.2}Co_{0.4}Fe_{0.4}O_{3-\delta}$ ceramic. Inset shows the Arrhenius plot of relaxation time obtain from the frequency dependent imaginary part of impedance for $La_{0.5}Sr_{0.5}Bi_{0.2}Co_{0.4}Fe_{0.4}O_{3-\delta}$ ceramic.

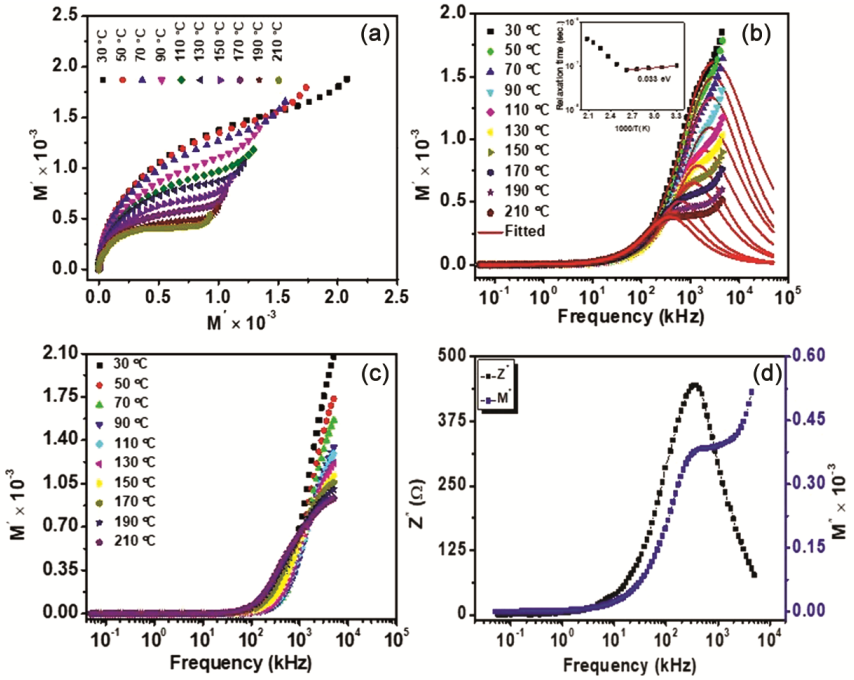

Fig. 5 — Figure.5-(a) The complex modulus plots for $La_{0.5}Sr_{0.5}Bi_{0.2}Co_{0\cdot4}Fe_{0.4}O_{3-\delta}$ ceramic in the temperature range 30-210 ℃. (b) The imaginary part of electric modulus (M´´) as function of frequency at different temperature for $La_{0.5}Sr_{0.5}Bi_{0.2}Co_{0\cdot4}Fe_{0.4}O_{3-\delta}$ ceramic. The solid line represents the fit of experimental M´´ data to the decay function. Inset shows the Arrhenius plot of relaxation time obtain from the frequency dependent imaginary part of electric modulus for $La_{0.5}Sr_{0.5}Bi_{0.2}Co_{0\cdot4}Fe_{0.4}O_{3-\delta}$ ceramic.(c) the real part of electric modulus (M´) as function of frequency at different temperature for $La_{0.5}Sr_{0.5}Bi_{0.2}Co_{0\cdot4}Fe_{0.4}O_{3-\delta}$ ceramic.

radius of arc is started to decease with the increasing of the temperature suggests that the conduction of electrons is mainly due to the hopping conduction between the oxygen ions and ferric/cobalt ions which is depend on the temperature[28, 35]. Figure 5 (b) represents the imaginary part of complex electric modulus ($M"$) as a function of frequency at selected temperature. These plots are characterized by the presence of peaks at the different temperature. The complex electric modulus *vs* frequency plots show the presence of single peak indicates that the appear peak is related to the grain boundary in the sample[35-37]. It is noticed that the peak position ($f"_{max}$) firstly move toward the higher frequency side and then shifts to the lower frequency side with the increasing of the temperature suggests that phase transition occurred in the $La_{0.5}Sr_{0.5}Bi_{0.2}Co_{0\cdot5\text{-}}Fe_{0.3}O_{3-\delta}$ ceramic sample above the 90 ℃ temperature. The observed peak in $M"\ vs\ f$ plots is associated to the conductivity relaxation phenomena of electrons those involve in the double exchange between the oxygen ions and ferric/cobalt ions in the $La_{0.5}Sr_{0.5}Bi_{0.2}Co_{0\cdot5\text{-}}Fe_{0.3}O_{3-\delta}$ ceramic sample and indicates the transition from long-range to short-range hopping conduction at the frequency where the peak is occurred with the increasing the temperature[36]. The shifting of the peak ($f"_{max}$) with the increasing of the temperature further evidence of a temperature-dependent hopping conduction of electrons in the overall electrical conduction (charge transport). Furthermore, the peak intensity of electric modulus ($M"_{max}$) is decreased with the increasing of the temperature suggests that the intensity of observed relaxation is thermally activated. The broadening of peak is increased with the increasing of the temperature reveals that an increase in the thermally activation of dipole in the material[35-37].

The logarithmic of the relaxation time ($\tau_{M''}$) as a function of the reciprocal temperature ($1/T$) extract from $M"\ vs\ f$ plots are presents in the inset of Fig. 5(b). The plot is expressed by Arrhenius's equation up to 90 ℃[38]:

$$\tau_{M''} = \tau_{oM''} exp\left[\frac{E_{a\tau M''}}{kT}\right] \qquad ...(8)$$

Where $E_{a\tau M''}$ is the activation energy for conductive relaxation and $\tau_{oM''}$ is characteristic relaxationtime. An unique value of the activation energy ($E_{a\tau M''}$) is found to 33 meV and characteristic relaxation time ($\tau_{oM''}$) is observed to 4.042 ×10 $^{-8}$ sec. in the temperature range 30 to 90 ℃.

The imaginary part of complex electric modulus as a function of frequency could be express in the terms of non-exponential decay function or Kolhrausch-Williams-Watts (KWW) parameter (β)[28, 39], which could be given as:

$$\phi(t) = exp\left(-\frac{t}{\tau_o}\right)^{\beta} \quad 0 < \beta < 1 \qquad ...(9)$$

Where, τ_o is the characteristic relaxation time constant and the function $\phi(t)$ represents the time evolution of the electric field. When the relaxation time distribution is increased then the stretched exponential parameter (β) is decreased *i.e.* the increasing of the broadening of peak gives rise to the decreasing value of stretched exponential parameter (β). When, $\beta \rightarrow 1$ suggests the single and ideal Debye type relaxation and $\beta \rightarrow 0$ indicates the multiple and non-Debye type relaxation (maximum interaction between the charge carriers)[28]. This could be extracted by fitting of the $M"\ vs\ f$ plots for each temperature as suggested method by Bergman *et al.*[40] Thus, this could be expressed:

$$M"(\omega) = M"_g(\omega) + M"_{gb}(\omega) \qquad ...(10)$$

$$M"_g(\omega) = \frac{M"_{gmax}}{(1-\beta_g) + \frac{\beta_g}{1+\beta_g}\left[\beta_g\left(\frac{\omega_{gmax}}{\omega}\right) + \left(\frac{\omega}{\omega_{gmax}}\right)^{\beta_g}\right]} \qquad ...(11)$$

$$M"_{gb}(\omega) = \frac{M"_{gbmax}}{(1-\beta_{gb}) + \frac{\beta_{gb}}{1+\beta_{gb}}\left[\beta_{gb}\left(\frac{\omega_{gbmax}}{\omega}\right) + \left(\frac{\omega}{\omega_{gbmax}}\right)^{\beta_{gb}}\right]} \qquad ...(12)$$

Where $M"_{gmax}$ and $M"_{gbmax}$ are the peak intensity associated to the grain interior and grain boundary and ω_{gmax} and ω_{gbmax} are the peak position corresponding to the grain interior and grain boundary, where the peak intensity $M"_{gmax}$ and $M"_{gbmax}$ are occurred, as well as β_g and β_{gb} are the KWW parameter associated to grain interior and grain boundary, respectively. We have used second term of the Eq. 8 to fit the experimental data because of single peak is observed in $M"\ vs\ f$ plots and presented as a solid line in Fig. 5 (b). The parameters obtained after fitting of second term of Eq. 8 are presented in Table 4. Furthermore, the observed value of KWW parameter (β) is less than unit and decreased with the increasing of the temperature reveals that the multiple and non-Debye type relaxation are occurred and the dependency of KWW parameter (β) on temperature suggests that the interaction between electrons those involve in double exchange is increased with the increasing of the temperature.

A combined plot of Z'' and $M"$ as a function of frequency gives the information of conduction relaxation process whether it is due to the long-range or short-range conduction of the charge carriers. Furthermore, if both peaks are occurred at same frequency then the conduction relaxation process is due to the long-range conduction of the charge carriers, otherwise the relaxation mechanism is because of the short-range conduction of the charge carriers[41]. Fig. 5(d) presents the combined plot of Z'' and $M"$ as a function of frequency for $La_{0.5}Sr_{0.5}Bi_{0.2}Co_{0.4}Fe_{0.4}O_{3-\delta}$ ceramic at temperature 210 ℃. In this figure, single peak of Z'' and $M"$is observed at the same frequency, which suggests that the conduction relaxation mechanism is due to the long-range conduction of charge carriers[42, 43].

Ac conductivity analysis

The ac conductivity has been analyzed as a function of the frequency (50 to 5 × $10^6 Hz$) in the

Table 4 — The fitting parameters obtained from Jonscher's double power law: dc conductivity (σ_{dc}), frequency independent constants (a and b), and exponents (n and m).

Temperature (°C)	σ_{dc} (× 10^{-4} S-cm^{-1})	a	b	n	m
30	3.01348	9.27875×10^{-9}	1.05623×10^{-13}	0.48501	1.42102
50	3.79909	9.30936×10^{-9}	1.15077×10^{-13}	0.40123	1.42510
70	4.19605	4.57195×10^{-9}	1.16584×10^{-13}	0.35123	1.43297
90	4.54777	5.14540×10^{-9}	1.54010×10^{-13}	0.28013	1.42957
110	4.45010	1.50527×10^{-8}	2.56817×10^{-13}	0.46950	1.39917
130	4.28915	2.57359×10^{-8}	2.73951×10^{-13}	0.44129	1.40128
150	3.88275	1.18079×10^{-8}	2.97166×10^{-13}	0.39533	1.40576
170	3.09100	6.14798×10^{-8}	1.68291×10^{-12}	0.29505	1.30482
190	2.61562	5.12130×10^{-8}	6.85150×10^{-12}	0.27117	1.21616
210	2.41266	3.72261×10^{-8}	5.84999×10^{-12}	0.25386	1.23065

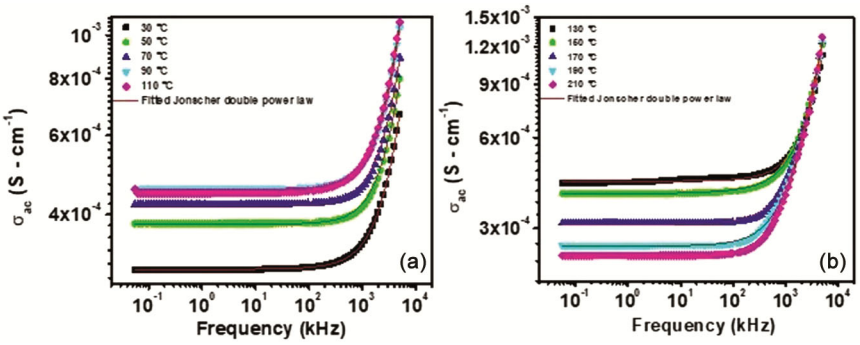

Fig. 6 — Ac conductivity for $La_{0.5}Sr_{0.5}Bi_{0.2}Co_{0.4}Fe_{0.4}O_{3-\delta}$ ceramic as a function of frequency in the temperature range (a) 30-110 ℃ and (b) 130-210 ℃. The solid line represents the fit of experimental ac conductivity data to Jonscher's double power law.

temperature range 30 to 210 ℃ for $La_{0.5}Sr_{0.5}Bi_{0.2}Co_{0.5}Fe_{0.3}O_{3-\delta}$ ceramic and presents in the Fig. 6 (a, b). Fig. 6 indicates that ac conductivity (σ_{ac}) is depend on frequency and follow the double power law relation at the high frequency region and a plateau is observed at the low frequency region. Furthermore, this type of behavior further indicates that a frequency independent part of conductivity (σ_{dc}) contributes to the total ac conductivity. Thus, the total ac conductivity could be explained by the following equation[44]:

$$\sigma_{ac} = \sigma_{dc} + a\omega^n + b\omega^m \quad ...(12)$$

Where σ_{dc} is dc conductivity mainly due to the excitation of charge carriers from localized states to the conduction bands and $a\omega^n + b\omega^m$ is typically the conduction due to the hopping of the charge carriers with "a" and "b" frequency independent constant and "n" and "m" are exponents with the values $0.0 < n < 1.0$ and $0.0 < m < 2.0$, respectively. Thus, the conduction behaviour is mainly depending on the conduction mechanism control by the hopping of the charge carriers (in this case, electrons those participate in double exchange between oxygen ions and ferric/cobalt ions). Furthermore, the value of ac conductivity is increased with the increasing of the temperature up to 90 ℃ and then starts to decreased with the increasing of the temperature from 110 to 210 ℃ is further evidence of phase transition, as discussed previously. Fitting of the experimental data yields the value of n and m, which suggests that dependence of n and m on temperature is a function of the conduction mechanism and tabulated in the Table 4.

Conclusion

In summary, the highly pure $La_{0.5}Sr_{0.5}Bi_{0.2}Co_{0.4}Fe_{0.4}O_{3-\delta}$ cathode ceramic powder was prepared by flash pyrolysis method and further conventional heat treatment for sintering. The Rietveld refinement of $La_{0.5}Sr_{0.5}Bi_{0.2}Co_{0.4}Fe_{0.4}O_{3-\delta}$ ceramic confirms rhombohedral crystal system with $R\bar{3}C$ space group symmetry. The microstructure of pellet sintered at 700 ℃ for 2 h shows bimodal type grain and porous nature. The deformed semi-circular arc in the Nyquist and complex electric modulus plots provides the information of the conduction process which is only due to the involvement of grain boundary. The activation energy corresponding to the impedance is almost equal to that determined using the electric modulus. The stretching constant (β) corresponding to grain boundary obtained from KWW (Kohlrausch-Williams-Watts) equation revels that the deviation towards the ideal Debye behavior as the temperature increases. The overlapping of relaxation peak in imaginary part of impedance and electric modulus reveals that conduction process is due to long-range motion of the charge carriers.

Acknowledgment

The authors are thankful to Prof. Debasis Bhattacharya, Materials Science Centre, IIT Kharagpur, India for providing synthesis facility and Prof. Neelam Srivastava, Department of Physics, MMV, Banaras Hindu University, Vanarsi, India for providing electrical measurement facility. Dr. Deepash Shekhar Saini also would like to thank UGC-India for the (Project No. UGC/SRG/No. F. 30-505/2020(BSR)) project funded under UGC-SRG program.

References

1 Xiong H, Liu H, Zhang R, Yu L, Zong Z, Zhang M & Li Z, *Int J Hydrogen Energy*, 44 (2019) 29733.
2 Damo U M, Ferrari M L, Turan A & Massardo A F, *Energy*, 168 (2019) 235.
3 Dhankhar S, Tiwari P, Baskar K, Basu S & Singh S, *Curr Appl Phys*, 17 (2017) 467.

4 Hossain S, Abdalla A M, Jamain S N B, Zaini J H & Azad A K, *Renew Sustain Energy Rev*, 79 (2017) 750.
5 Da Silv F S & de Souza T M, *Int J Hydrogen Energy*, 42 (2017) 26020.
6 Wang H, Zhang X, Zhang W, Wei Z, Guan K, Meng J & Liu X, *Int J Hydrogen Energy* 44 (2019) 13757.
7 Dwivedi S, *Int J Hydrogen Energy*, 44 (2020) 23988.
8 Zhu J H & Ghezel-Ayagh H, *Int J Hydrogen Energy*, 42 (2017) 24278.
9 Liu Y, Meng X, Yu F, Yin M, Yang N, Meng B & Liu S, *Int J Hydrogen Energy*, 43 (2018) 12328.
10 Jacobs R, Mayeshiba T, Booske J & Morgan D, *Adv Energy Mater*, 8 (2018).
11 Qiu L, Ichikawa T, Hirano A, Imanishi N & Takeda Y, *Solid State Ion*, 158 (2003) 55.
12 Skinner S J, *Int J Inorg Mater*, 3 (2001) 113.
13 Jiang S P, *Solid State Ion*, 146 (2002) 1.
14 Tu H Y, Takeda Y, Imanishi N & Yamamoto O, *Solid State Ion*, 100 (1997) 283.
15 Sunarso J, Motuzas J, Liu S & Costa J C D, *J Membr Sci*, 361 (2010) 120.
16 Li S, Cong Y, Fang L, Yang W, Lin L & Meng J, *Mater Res Bull*, 33 (1998)183.
17 Shao Z, Xiong G, Cong Y & Yang W*, J Membr Sci*, 164 (2000) 167.
18 Saini D S, Ghosh A, Tripathy S, Kumar A, Sharma S K, Kumar N, Majumdar S & Bhattacharya D, *Sci Rep,* 10 (2020) 3461.
19 Singh S, Kumar A & Saini D S, *Solid State Tech*, 63 (2020) 13367.
20 Ten Elshof J E & Boeijsma J, *Powder diffr*, 11 (1996) 240.
21 Barsoukov E & Macdonald J R, Impedance spectroscopy: theory, experiment, and applications, John Wiley & Sons, (2005).
22 West A R, Sinclair D C & Hirose N, *J Elect*, 1 (1997) 65.
23 Chen Y C, *J Mar Sci Tech*, 15 (2007) 307.
24 Guo X & Waser R, *Prog Mater Sci*, 51 (2006) 151.
25 Srinivas K & James A R, *J Appl Phys*, 86(1999) 3885.
26 Saini D S, Ghosh A, Tripathy S, Kumar A, Sharma S K & Bhattacharya D, *ACS Appl Energy Mater,* 1 (2018) 3469.
27 Majhi K, Varma K B R & Rao K J, *J Appl Phys*, 106 (2009) 084106.
28 Saini D S, Tripathy S, Kumar A, Sharma S K, Ghosh A & Bhattacharya D, *Ionics*, 24 (2018) 1161.
29 Wynblatt P & Rohrer G S, *J Eur Ceram Soc*, 23 (2003) 2841.
30 Ünal B, Almessiere M, Korkmaz A D & Slimani Y, *J Rare Earth*, 38 (2020) 1103.
31 Zener C *Phys Rev*, 82 (1951) 403.
32 Zhang M F, Wang Y, Wang K F, Zhu J S & Liu J M, *J Appl Phys*, 105 (2009) 061639.
33 Mahajan S, Thakur O P, Bhattacharya D K & Sreenivas K, *J Phys D Appl Phys*, 42 (2009) 065413.
34 Andoulsi-Fezei R, Nasr S, Karima H-N & Mokhtar F, *J Asian Ceram Soc*, 8 (2020) 94.
35 Sinclair DC & West AR, *J Mater Sci*, 29 (1994) 6061.
36 Hodge I M, Ingram M D & West A R, *J Electroanal Chem Interfacial Electrochem*, 74 (1976) 125.
37 Patel H K & Martin S W, *Solid State Ionics*, 53 (1992) 1148.
38 Tiwaria B, Babua T & Choudhary R N P, *Mater Chem Phys*, 256 (2020) 123665.
39 Howell F S, Bose R A, Macedo P B & Moynihan C T, *J Phys Chem*, 78 (1974) 639.
40 Bergman R, *J Appl Phys*, 88 (2000) 1356.
41 Ke Q, Lou X, Wang Y & Wang J, *Phys Rev B*, 82 (2010) 024102.
42 Gerhardt R, *J Phys Chem Solids*, 55 (1994) 1491.
43 Manzoor S, Husain S, Somvanshi A & Fatema M*, J Appl Phys*, 128 (2020) 064101.
44 Moualhi Y, Nofal M M, M'nassri R, Rahmouni H, Selmi A, Gassoumi M & Cheikrouhou A, *Ceram Int*,46 (2020) 1601.